Opto-Electronic Science

CN 51−1800/O4 ISSN 2097−0382 (Print) ISSN 2097−4000 (Online)

Photoacoustic spectroscopy and light-induced thermoelastic spectroscopy based on inverted-triangular lithium niobate tuning fork

Junjie Mu, Guowei Han, Runqiu Wang, Shunda Qiao, Ying He and Yufei Ma

Citation: Mu JJ, Han GW, Wang RQ, et al. Photoacoustic spectroscopy and light-induced thermoelastic spectroscopy based on inverted-triangular lithium niobate tuning fork. *Opto-Electron Sci* **4**, 250035 (2025).

https://doi.org/10.29026/oes.2025.250035

Received: 31 August 2025; Accepted: 26 November 2025; Published online: 17 December 2025

Related articles

Highly sensitive laser spectroscopy sensing based on a novel four-prong quartz tuning fork
Runqiu Wang, Shunda Qiao, Ying He, Yufei Ma
Opto-Electronic Advances 2025 **8**, 240275 doi: 10.29026/oea.2025.240275

Agile cavity ringdown spectroscopy enabled by moderate optical feedback to a quantum cascade laser
Qinxue Nie, Yibo Peng, Qiheng Chen, Ningwu Liu, Zhen Wang, Cheng Wang, Wei Ren
Opto-Electronic Advances 2024 **7**, 240077 doi: 10.29026/oea.2024.240077

Highly sensitive and real-simultaneous CH_4/C_2H_2 dual-gas LITES sensor based on Lissajous pattern multi-pass cell
Haiyue Sun, Ying He, Shunda Qiao, Yahui Liu, Yufei Ma
Opto-Electronic Science 2024 **3**, 240013 doi: 10.29026/oes.2024.240013

High fiber-to-fiber net gain in erbium-doped thin film lithium niobate waveguide amplifier as an external gain chip
Jinli Han, Mengqi Li, Rongbo Wu, Jianping Yu, Lang Gao, Zhiwei Fang, Min Wang, Youting Liang, Haisu Zhang, Ya Cheng
Opto-Electronic Science 2025 **4**, 250004 doi: 10.29026/oes.2025.250004

More related article in Opto-Electronic Journals Group website

Opto-Electronic Science

Article

December 2025, Vol. 4, No. 12

DOI: 10.29026/oes.2025.250035 CSTR: 32246.14.oes.2025.250035

Photoacoustic spectroscopy and light-induced thermoelastic spectroscopy based on inverted-triangular lithium niobate tuning fork

Junjie Mu[1,2], Guowei Han[3], Runqiu Wang[1,2], Shunda Qiao[1,2], Ying He[1,2] and Yufei Ma[1,2]*

In this paper, a novel self-designed inverted-triangular lithium niobate tuning fork (LiNTF) was used to construct gas sensing system for the first time. The optimal ratio of the upper and lower boundaries of the inverted-triangular LiNTF is found by scanning through finite element analysis (FEA). The surface charge density and stress value of the inverted-triangular LiNTF are both higher than those of the standard quartz tuning fork (QTF). In the lithium niobate-enhanced photoacoustic spectroscopy (LiNPAS) sensing system, the 2*f* peak and signal-to-noise ratio (SNR) of the inverted-triangular LiNTF are 7.41 times and 5.89 times those of the standard QTF, respectively. After forming acoustic standing wave field with the acoustic micro-resonator (AmR), the LiNPAS system achieves an SNR 56.16 times higher than without the AmR. Based on Allan variance analysis, the system achieves a minimum detection limit (MDL) of 7.25 ppb with an averaging time of 800 seconds. In the light-induced thermoelastic spectroscopy (LITES) sensing system, the 2*f* peak and SNR of the inverted-triangular LiNTF are 7.82 times and 6.03 times those of the standard QTF, respectively. When the averaging time reaches 100 s, the MDL of the system is found to be 25.78 ppb.

Keywords: lithium niobate tuning fork; lithium niobate-enhanced photoacoustic spectroscopy; light-induced thermoelastic spectroscopy; C_2H_2 detection

Mu JJ, Han GW, Wang RQ et al. Photoacoustic spectroscopy and light-induced thermoelastic spectroscopy based on inverted-triangular lithium niobate tuning fork. *Opto-Electron Sci* **4**, 250035 (2025).

Introduction

Trace gas detection technology is a widely used analytical method with applications in atmospheric monitoring, petrochemical industries, agricultural management, and medical diagnostics[1−9]. Laser spectroscopy-based trace gas detection offers advantages such as rapid response, high sensitivity, and low background noise[10−17]. Photoacoustic spectroscopy (PAS), a technique based on the photoacoustic effect, typically employs a microphone as the acoustic wave transducer[18−20]. However, microphone-based PAS has several drawbacks, including a large footprint and susceptibility to environmental interference. To address these issues, quartz-enhanced photoacoustic spectroscopy (QEPAS) was proposed in 2002[21], replacing the microphone in traditional PAS with a quartz tuning fork (QTF). The QTF converts acoustic signals from the photoacoustic effect into electrical signals via its piezoelectric effect. Due to the millimeter-scale size, low

[1]National Key Laboratory of Laser Spatial Information, Harbin Institute of Technology, Harbin 150001, China; [2]Zhengzhou Research Institute, Harbin Institute of Technology, Zhengzhou 450008, China; [3]Engineering Research Center for Semiconductor Integrated Technology, Institute of Semiconductors, Chinese Academy of Sciences, Beijing 100083, China.

*Correspondence: YF Ma, E-mail: mayufei@hit.edu.cn

Received: 31 August 2025; Accepted: 26 November 2025; Published online: 17 December 2025

cost, narrow response band, and high *Q*-factor of QTF[22–27], QEPAS technology offers advantages such as compact size, economical, and excellent noise immunity[28–34]. However, QEPAS technology still has certain limitations, such as the requirement for contact measurement. When the QTF is directly exposed to corrosive gases, it is highly prone to corrosion and damage[35]. To address this issue, in 2018, Ma et al. proposed light-induced thermoelastic spectroscopy (LITES). This technique enables non-contact measurement by using laser excitation to induce thermoelastic vibrations in the QTF after the light passes through a gas cell[36–42]. This feature allows LITES to demonstrate unique advantages in specialized applications, including corrosive gas analysis and combustion environment monitoring[43–49].

The QTF plays a crucial role as a detector in both QEPAS and LITES. Its performance directly determines the detection capabilities of these two systems[50–54]. However, the commercially available standard QTFs are not originally designed for these techniques, leaving significant room for performance optimization[55]. When subjected to mechanical stress, the QTF deforms and generates charges due to the piezoelectric effect. The α-quartz used in commercial QTFs has a relatively low piezoelectric coefficient d_{11} of only 2.3 pC/N. Therefore, selecting materials with higher piezoelectric coefficients can significantly enhance the surface charge density under the same stress conditions[56–58]. Lithium niobate ($LiNbO_3$), an important ferroelectric crystal, exhibits remarkable piezoelectric effects (6–70 pC/N) across different crystal orientations[59]. Additionally, materials with higher electromechanical coupling coefficients produce larger output signal amplitudes under identical external conditions. $LiNbO_3$ has a coupling coefficient of 0.68, compared to quartz's 0.3, making it a superior choice for improving signal strength[60–65]. Furthermore, the high resonant frequency (f_0=32768 Hz) results in limited energy accumulation time and poor detection performance. Recently, Cantatore et al. conducted research using $LiNbO_3$ tuning fork (LiNTF) as a photoacoustic spectroscopy detector. The experimental results show that the minimum detectable limit (MDL) of LiNTF measured in water vapor is 30 ppm, while that of the standard QTF is 26 ppm, with no significant difference between the two[66]. This may be attributed to the fact that only single-sided electrodes were coated on the surface of LiNTF, the shape of LiNTF was not optimized, and the excessively high resonance frequency led to insufficient time for energy accumulation.

This paper presents, for the first time, gas sensing utilizing a novel self-designed inverted-triangular $LiNbO_3$ tuning fork (LiNTF). Through finite element analysis of the optimal upper-to-lower boundary ratio, the stress distribution and surface charge characteristics of the LiNTF were optimized. To validate its detection performance, a $LiNbO_3$ photoacoustic spectroscopy (LiNPAS) system and a LITES system were established. Acetylene (C_2H_2), a representative petrochemical industry gas, was selected as the target analyte to evaluate the performance of the inverted-triangular LiNTF-based sensors.

LiNTF simulation

To simulate the performance of a LiNTF, a finite element model using COMSOL software was constructed by coupling multiple physical fields, including the Solid Mechanics module, Electrostatics module, heat transfer in Solids module, and Optics module. For the LiNPAS simulation, a line sound source passing through the gap between the prongs was built in a spherical air cavity. The line sound source was loaded with the LiNTF's f_0 to simulate the acoustic waves generated by the periodic thermal expansion of gas caused by the modulated light beam passing through the gas. Excess acoustic waves were absorbed by the perfectly matched layer on the outer wall of the spherical cavity. To obtain the optimal inverted triangular shape, simulations were conducted by adjusting the ratio of the lower boundary to the upper boundary of the prongs, and charge integration was performed over all surfaces of the LiNTF. The results are shown in Fig. 1, as the ratio increases, the total charge value of the LiNTF rises slowly, reaching a maximum of 6.2963×10^{-8} C when the ratio reaches 0.68, and then begins to decrease. It can be concluded that the inverted-triangular shape can amplify the vibration amplitude of the LiNTF during oscillation, thereby enhancing the signal amplitude. However, an excessively small ratio will reduce the surface area of the LiNTF, leading to a decrease in the total charge amount.

The cut type with the largest piezoelectric coefficient of the $LiNbO_3$ crystal is selected, namely the 128° rotated *y*-axis cut, the thickness is 0.3 mm, the same as that of the standard QTF. An inverted-triangular LiNTF model with an optimal lower-to-upper boundary ratio of 0.68 was developed. Figure 2(a) and 2(b) present the dimensional geometries for the standard QTF and the optimized inverted-triangular LiNTF, respectively. The

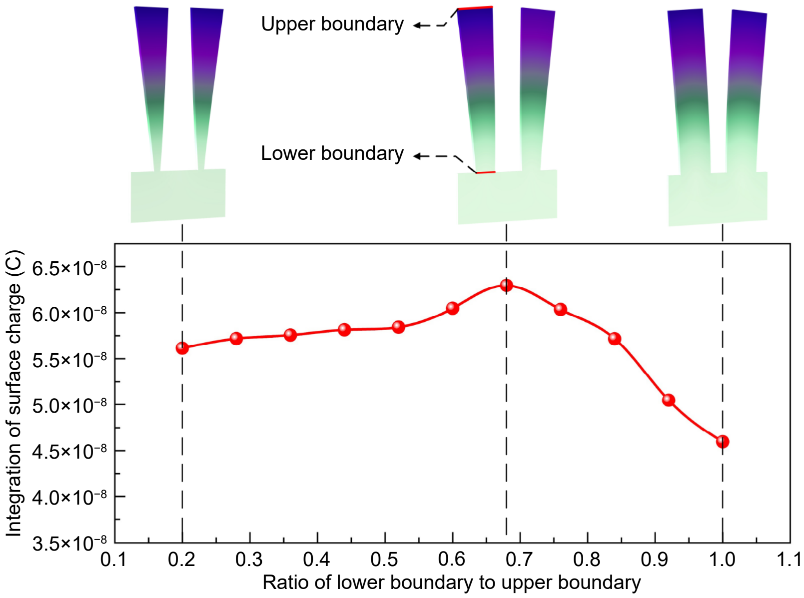

Fig. 1 | Relationship between the ratio of the lower boundary to the upper boundary of LiNTF and the surface charge integration.

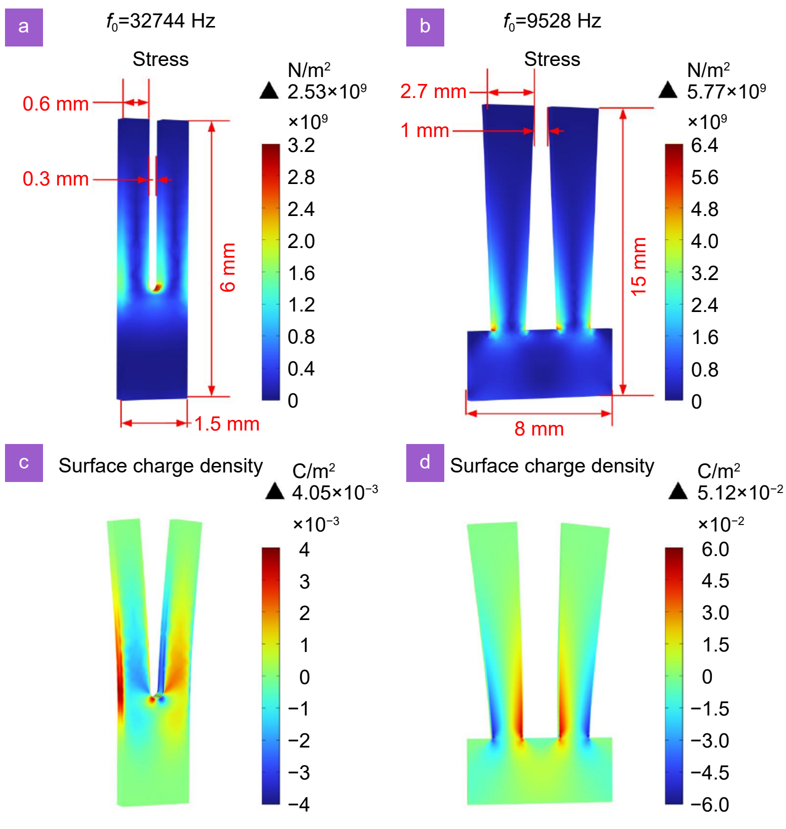

Fig. 2 | Surface charge and stress distribution in LiNPAS simulation. (**a**) Stress distribution and dimensions of the standard QTF. (**b**) Stress distribution and dimensions of the inverted-triangular LiNTF. (**c**) Surface charge distribution of the standard QTF. (**d**) Surface charge distribution of the inverted-triangular LiNTF.

eigenfrequency analysis reveals that the fundamental f_0 is 32744 Hz for the standard QTF and 9528 Hz for the optimized inverted-triangular LiNTF. The surface stress distributions are also presented in Fig. 2(a) and 2(b), respectively, for the LiNPAS simulation. The maximum surface stress values of 2.53×10⁹ N/m² (standard QTF) and 5.77×10⁹ N/m² (LiNTF) demonstrate a 2.28-fold stress enhancement in the LiNTF design. Notably, the

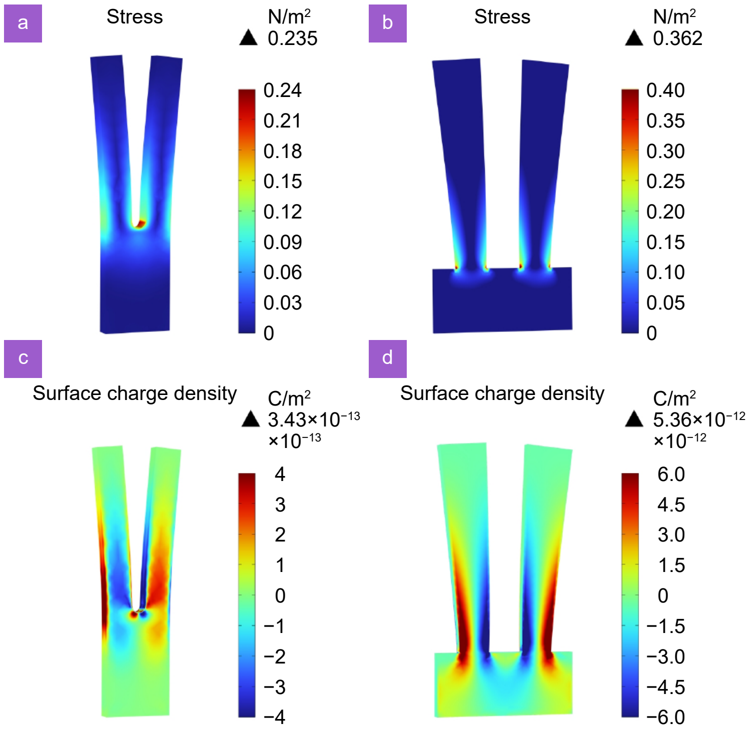

Fig. 3 | Surface charge and stress distribution in LITES simulation. (**a**) Stress distribution of the standard QTF. (**b**) Stress distribution of the inverted-triangular LiNTF. (**c**) Surface charge distribution of the standard QTF. (**d**) Surface charge distribution of the inverted-triangular LiNTF.

inverted-triangular LiNTF exhibits more concentrated stress distribution at the prong roots compared to the standard QTF. Figure 2(c) and 2(d) show the charge distribution diagrams of the standard QTF and the inverted-triangular LiNTF, respectively. The maximum surface charge density of the standard QTF is 4.05×10^{-3} C/m², while that of the inverted-triangular LiNTF is 5.12×10^{-2} C/m², which is 12.64 times higher than that of the standard QTF. Unlike the symmetric arrangement of positive and negative charges on the entire standard QTF, the positive and negative charges of the inverted-triangular LiNTF are symmetrically distributed on each prong.

To simulate the performance of LiNTF in LITES sensing technology, a multi-physics coupling model was established by integrating the Solid Mechanics, Electrostatics, Heat Transfer in Solids, and Geometric Optics modules. A spatial light beam was configured to irradiate the root of the LiNTF prongs, and a modulation signal matching the in-plane vibration resonant frequency of the LiNTF was applied to the spatial light to induce thermoelastic vibrations in the LiNTF. The stress distributions of the standard QTF and the inverted-triangular LiNTF are shown in Fig. 3(a) and 3(b), respectively. The LiNTF exhibits a maximum stress value 1.54 times greater than that of the standard QTF. Their surface charge distributions are illustrated in Fig. 3(c) and 3(d). The surface charge distributions of the two tuning forks in the LITES system match those in QEPAS. However, the inverted-triangular LiNTF achieves a maximum surface charge density 15.63 times greater than that of the standard QTF.

Experimental setup

The experimental sensor system configuration is illustrated in Fig. 4. A single-mode distributed feedback (DFB) diode laser with a wavelength of 1530.37 nm, an output power of 15 mW, and a linewidth of 1 MHz was used as the light source, and the absorption line of C_2H_2 at 6534.56 cm^{-1} was selected for detection. The DFB laser beam was collimated using a fiber collimator (FC). A low-frequency sawtooth wave signal generated by a signal generator and a high-frequency sine wave signal generated by a lock-in amplifier were loaded into the laser controller to modulate the DFB laser, where the frequency of the high-frequency sine wave signal was set to $f_0/2$. Wavelength modulation spectroscopy and second harmonic technology are employed to suppress background noise. As shown in Fig. 4(a), in the C_2H_2-LiNPAS system, the laser was focused by a lens, passed through a

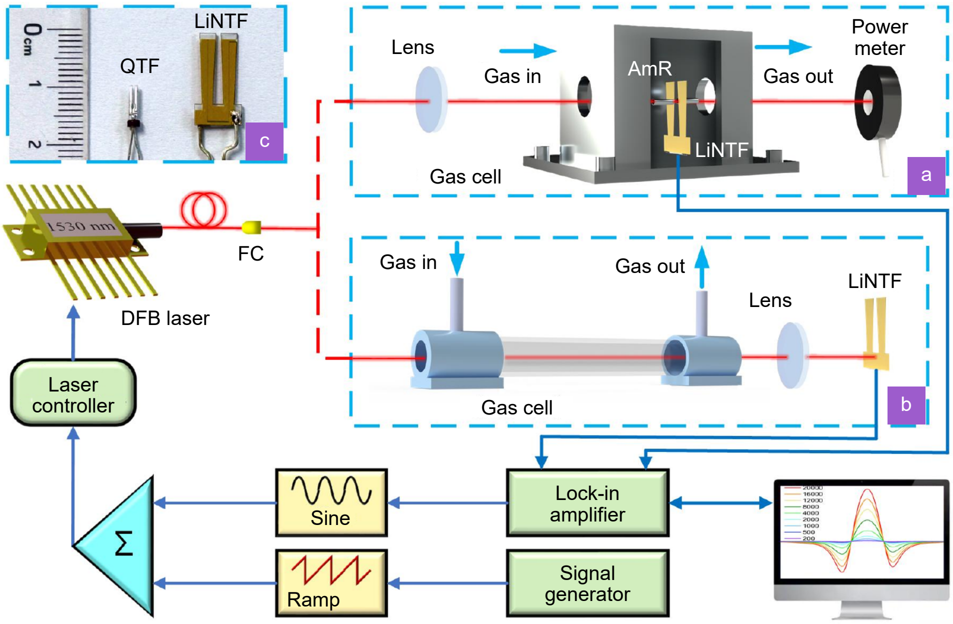

Fig. 4 | Schematic diagram of the C_2H_2 sensor. (**a**) C_2H_2-LiNPAS system. (**b**) C_2H_2-LITES system. (**c**) Schematic diagram of the standard QTF and the inverted-triangular LiNTF.

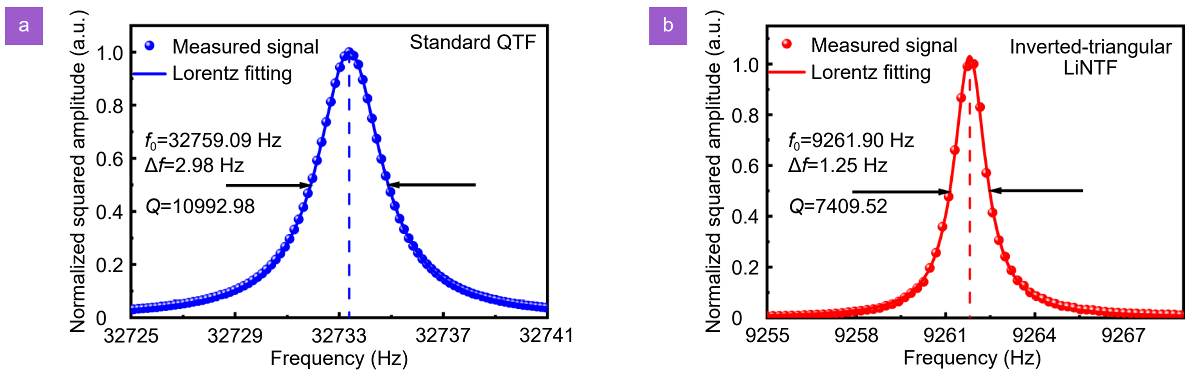

Fig. 5 | Frequency characteristic curves of the standard QTF and the inverted-triangular LiNTF. (**a**) The standard QTF. (**b**) The inverted-triangular LiNTF.

wedge-shaped lens, and then enters the gas cell filled with the target gas. Use a mass flow controller (MFC) to prepare C_2H_2 with different concentrations. After passing through the acoustic micro-resonator (AmR) and the gap between the prongs of the inverted-triangular LiNTF, it irradiated the power meter. The power meter was used for optical adjustment of the system. In the C_2H_2-LITES system, as shown in Fig. 4(b), the laser passed through a gas cell with an optical path length of 20 cm and was then focused by a lens onto the root of the prongs of the inverted-triangular LiNTF. The signal generated by the inverted-triangular LiNTF was transmitted to a lock-in amplifier for the second harmonic demodulation to obtain the 2*f* signal. The physical images of the standard QTF and inverted-triangular LiNTF used in the experiment are shown in Fig. 4(c).

Experimental results and discussion

Performance of LiNPAS sensor based on the inverted-triangular LiNTF

Firstly, the frequency response characteristics of the standard QTF and inverted-triangular LiNTF were measured using an optical excitation method. A lock-in amplifier was used to continuously modulate the laser frequency to generate light at different frequencies. The resonant frequency f_0 was determined when the electrical signal reached its peak, as shown in Fig. 5. Figure 5(a) depicts the frequency response curve of the standard QTF, with the peak frequency and bandwidth (Δf) measured as 32759.09 Hz and 2.98 Hz, respectively. Based on

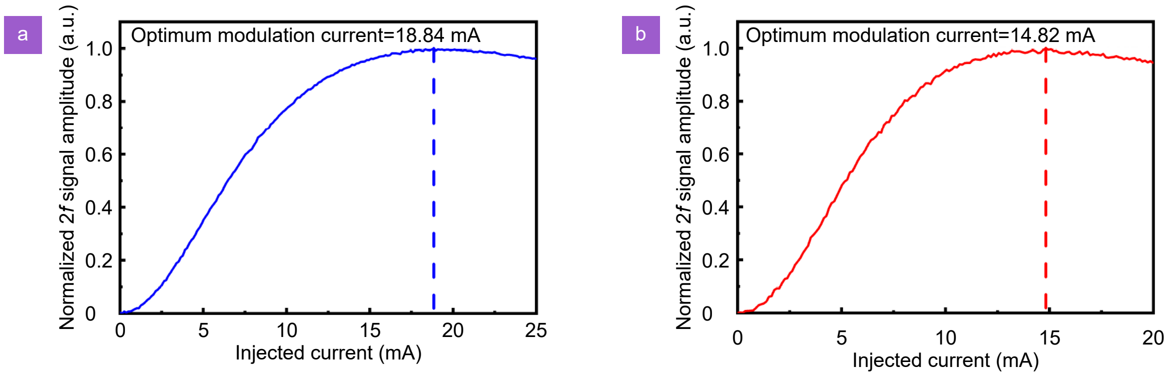

Fig. 6 | The optimization of modulation depth. (**a**) The standard QTF. (**b**) The inverted-triangular LiNTF.

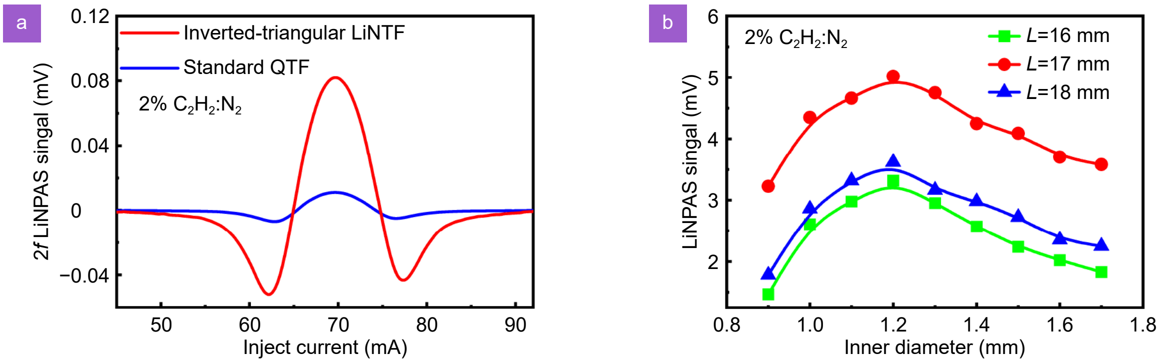

Fig. 7 | (**a**) 2*f* signals of C_2H_2-QEPAS system based on the standard QTF and C_2H_2-LiNPAS systems based on the inverted-triangular LiNTF. (**b**) Relationship between the 2*f* peak value of the C_2H_2-LiNPAS, inner diameter and tube length.

the quality factor (Q) calculation formula $Q = f_0/\Delta f$, the Q value of the standard QTF was determined as 10992.98. Similarly, as shown in Fig. 5(b), the inverted-triangular LiNTF exhibited f_0 = 9261.90 Hz and Δf = 1.25 Hz, producing a Q value of 7409.52. The lower resonant frequency of the LiNTF enhances energy accumulation, while the narrower bandwidth helps suppress noise. Notably, there is a deviation between the measured f_0 and COMSOL simulation results. This discrepancy arises because the simulation did not account for frequency shifts caused by surface electrodes or performance changes due to mounting the LiNTF on the base.

The influence of modulation current on signal amplitude was studied by varying its magnitude, and the results are shown in Fig. 6. As the modulation current increases, the signal amplitude first rises rapidly and then decrease gradually after reaching its peak. The modulation current for the standard QTF to reach the maximum signal amplitude is 18.84 mA as shown in Fig. 6(a), while that for the inverted-triangular LiNTF is 14.82 mA as shown in Fig. 6(b).

In the C_2H_2-LiNPAS system, the modulated laser interacts with gas molecules, generating acoustic signals that drive the LiNTF vibration. The measured results are shown in Fig. 7(a), the 2*f* peak signal of the standard QTF can reach 11.06 μV, while that of the inverted-triangular LiNTF is 81.96 μV. It can be seen that the signal of the inverted-triangular LiNTF is enhanced by 7.41 times compared to the standard QTF. This indicates that the high piezoelectric coefficient of $LiNbO_3$ significantly improves the signal amplitude, and the special shape of the inverted-triangular LiNTF also significantly increases the vibration amplitude of the LiNTF, thereby enhancing the signal amplitude.

The AmR allows the acoustic waves to form a standing wave field, causing resonance enhancement of the acoustic signals within the AmR to increase the vibration amplitude of the LiNTF and boost the electrical signal amplitude. To achieve the optimal coupling effect of the AmR, a microscope was used to adjust the distance between the two AmRs and the LiNTF to approximately 50 μm. The tube length L of the AmR for the optimal enhancement of acoustic signals should follows $\lambda_s/4<L<\lambda_s/2$, where λ_s is the wavelength of the acoustic wave. The inner diameter of the AmR also affects the amplitude of acoustic signals, so the tube length and inner diameter

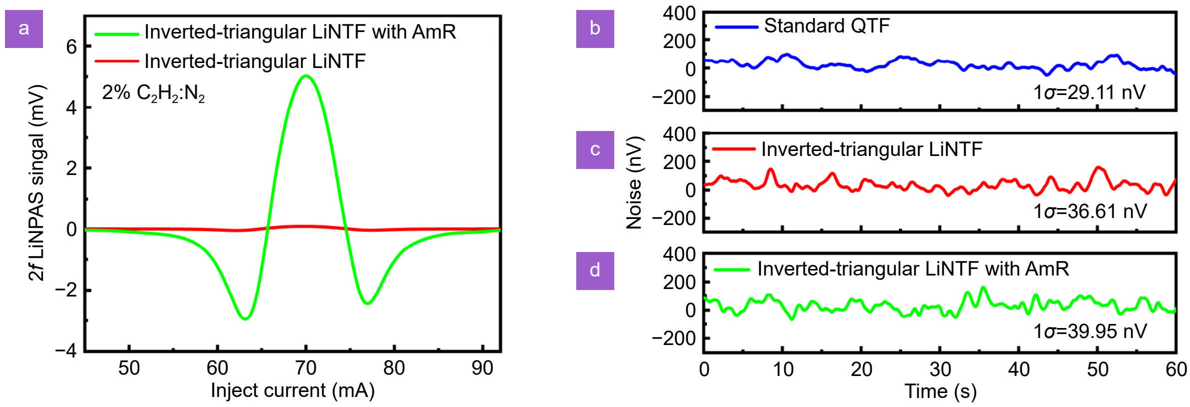

Fig. 8 | (**a**) 2*f* signals of C_2H_2-LiNPAS systems based on the inverted-triangular LiNTF with and without AmR. (**b**) Noise of the standard QTF. (**c**) Noise of the inverted-triangular LiNTF without AmR. (**d**) Noise of the inverted-triangular LiNTF with AmR.

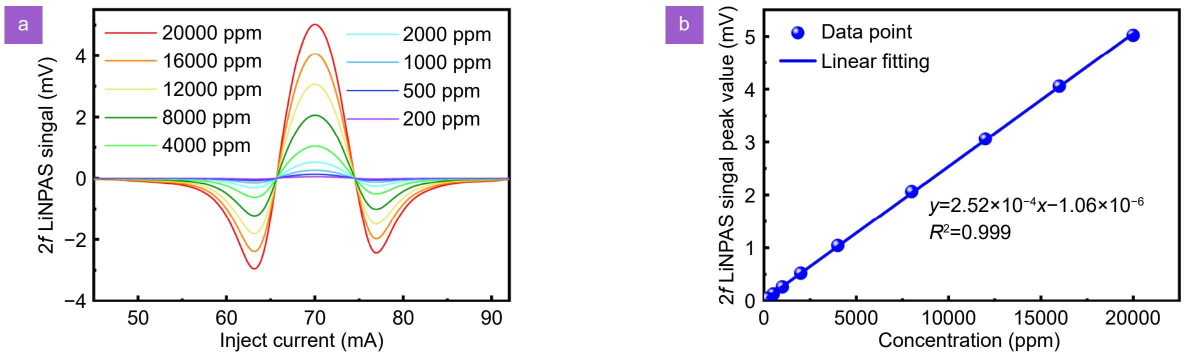

Fig. 9 | C_2H_2-LiNPAS system with AmR. (**a**) 2*f* signals of C_2H_2 at different concentrations. (**b**) Linear fitting of 2*f* signal peaks.

dimensions of the AmR were optimized as shown in Fig. 7(b). Experimental data shows that in a 20000 ppm C_2H_2 environment at standard atmospheric pressure and room temperature, the optimal tube length is 17 mm and the inner diameter is 1.2 mm. Using this AmR for subsequent LiNPAS experiments and comparing it with LiNPAS without AmR, as shown in Fig. 8(a), the 2*f* peak signals are 81.96 μV and 5.02 mV respectively. It can be seen that the presence of AmR enhances the signal by 61.25 times compared to the absence of AmR. In a pure N_2 environment, the noise standard deviations of the C_2H_2-QEPAS based on the standard QTF and C_2H_2-LiNPAS based on the inverted-triangular LiNTF with and without AmR are measured as shown in Fig. 8(b–d), which are 29.11 nV, 36.61 nV, 39.95 nV respectively. The signal-to-noise ratios (SNR) for the three systems were calculated as 379.94, 2238.73, 125657.07, and the corresponding minimum detection limits (MDL) were calculated as 52.64 ppm, 8.93 ppm, 0.16 ppm. The MDL of the inverted-triangular LiNTF is improved by 5.89 times compared to the standard QTF, and the inverted-triangular LiNTF with AmR is improved by 56.16 times compared to that without AmR.

Measurements of C_2H_2 concentrations ranging from 200 ppm to 20000 ppm were performed using the LiNTF system with an AmR configuration. The obtained 2*f* signals are presented in Fig. 9(a). After linear fitting, as showing in Fig. 9(b), the signal peaks exhibit outstanding linearity with a *R*-square value of 0.999. This indicates that the LiNPAS system demonstrates excellent linear concentration response.

The Allan variance analysis was performed on the system. The system was continuously monitored for 12 hours in a pure nitrogen environment with a 1 s interval between sampling points, and the results show that the system has excellent long-term stability. The obtained results are shown in Fig. 10. At an averaging time of 800 s, the standard QTF system achieves an MDL of 1.75 ppm; the inverted-triangular LiNTF system reaches an MDL of 281.85 ppb; the inverted-triangular LiNTF system with AmR attains an MDL of 7.25 ppb. These results indicate that all three systems exhibit excellent long-term stability.

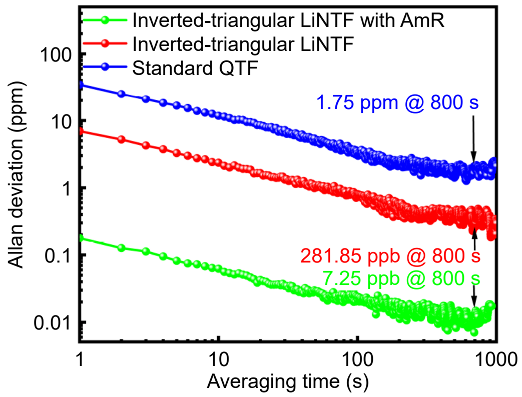

Fig. 10 | | Allan variance of the standard QTF, the inverted-triangular LiNTF and the inverted-triangular LiNTF with AmR based PAS systems.

Performance of LITES sensor based on the inverted-triangular LiNTF

A C_2H_2-LITES system was built to further verify the LiNTF's performance. The laser beam, after being absorbed by a 20000 ppm C_2H_2 gas, was focused on the root of the inverted-triangular LiNTF. Due to its higher piezoelectric coefficient and thermal expansion coefficient compared to quartz, LiNTF can generate greater deformation and surface charge under the same conditions. The measured results are shown in Fig. 11(a), the $2f$ peak signal of the inverted-triangular LiNTF can reach 6.13 mV, while that of the standard QTF is 0.784 mV. The noise in a pure N_2 environment was also measured, as shown in Fig. 11(b) and 11(c). The noise values of the standard QTF and the inverted-triangular LiNTF are 62.05 nV and 80.30 nV, respectively. The calculated SNRs are 12634.97 and 76338.73, resulted in MDLs of 1.58 ppm and 0.26 ppm, respectively. The detection capability of the LITES system with the inverted-triangular LiNTF is improved by 6.03 times compared to that with the standard QTF.

Concentration response was conducted on the LITES system under different C_2H_2 concentrations ranging from 200 ppm to 20000 ppm. The obtained $2f$ signals are shown in Fig. 12(a). Figure 12(b) demonstrates a strong linear correlation (R^2 = 0.999) between the $2f$ signal amplitude and C_2H_2 concentration, confirming excellent linear response performance of the inverted-triangular LiNTF-based LITES system.

To verify the long-term stability of the system, Allan deviation analysis were performed on the LITES systems with the standard QTF and the inverted-triangular LiNTF in a pure N_2 environment. The measured results are shown in Fig. 13. In Fig. 13(a), when the averaging time reaches 100 s, the MDL of the LITES system with the standard QTF reached 177.25 ppm. In Fig. 13(b), the MDL of the LITES system with the inverted-triangular LiNTF improved to 25.78 ppm at the averaging time reaches 100 s.

Conclusions

In this paper, a novel self-designed inverted-triangular LiNTF was used to construct gas sensing system for the first time. Benefiting from its excellent piezoelectric coefficient and electromechanical coupling coefficient, LiNTF can generate more surface charges compared with the standard QTF. Simulations were conducted by controlling the ratio of the lower boundary to the upper boundary of the LiNTF to find the optimal inverted triangular shape, and it was verified that both the surface charge density and stress value of the LiNTF are significantly superior to those of the standard QTF. C_2H_2-LiNPAS and C_2H_2-LITES systems were built to perform

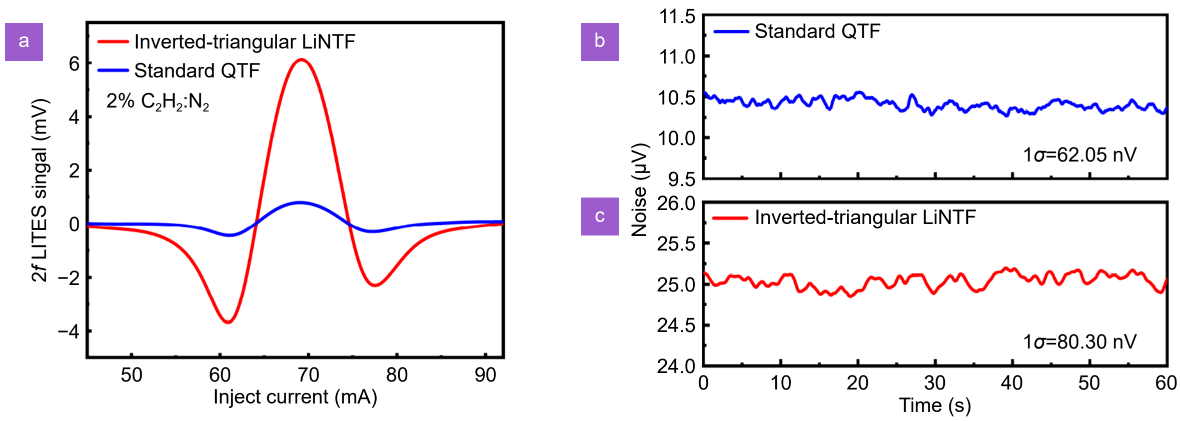

Fig. 11 | (**a**) $2f$ signals of C_2H_2-LITES systems with the standard QTF and the inverted-triangular LiNTF. (**b**) Noise of the standard QTF. (**c**) Noise of the inverted-triangular LiNTF.

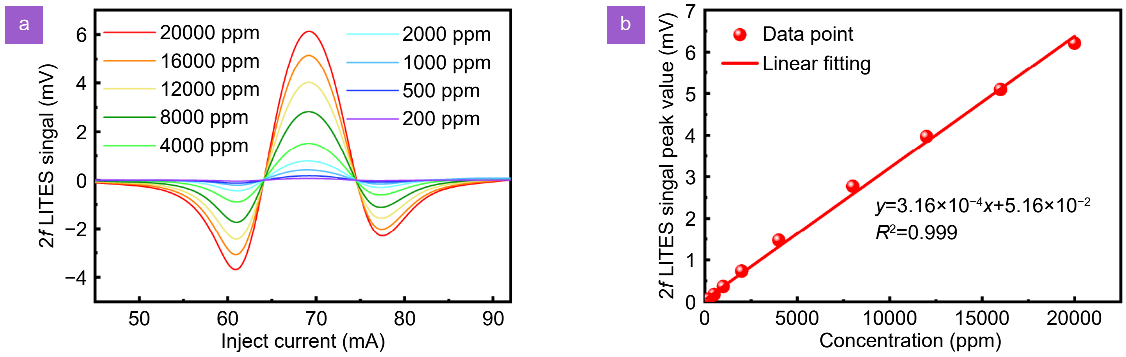

Fig. 12 | C_2H_2-LITES system. (**a**) 2*f* signals of C_2H_2 at different concentrations. (**b**) Linear fitting of 2*f* signal peaks.

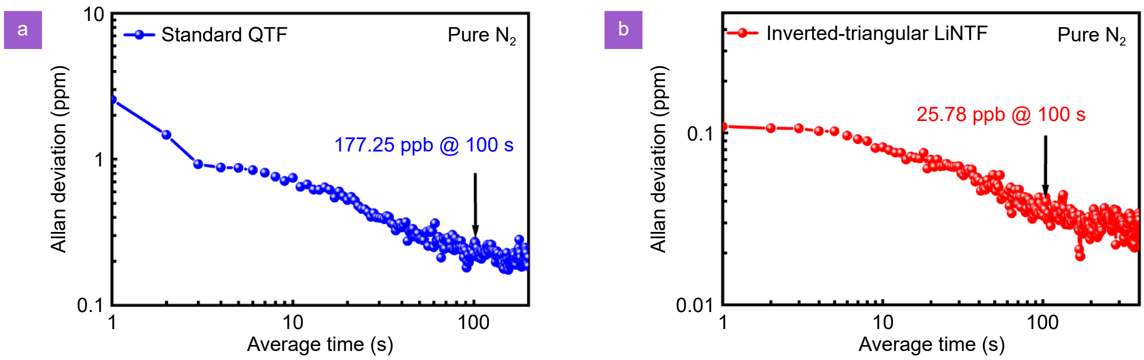

Fig. 13 | Allan variance of the two C_2H_2-LITES systems. (**a**) The standard QTF. (**b**) The inverted-triangular LiNTF.

experimental investigations. In the C_2H_2-LiNPAS system, the inverted-triangular LiNTF achieved a 5.89-fold improvement in SNR compared to the standard QTF. With the addition of AmR, the SNR was further enhanced by 56.16 times. Allan deviation analysis confirmed the system's long-term stability, yielding a MDL of 7.25 ppb at an averaging time of 800 s. In the C_2H_2-LITES system, the inverted-triangular LiNTF demonstrated a 6.03-fold higher SNR compared to the standard QTF. With an averaging time of 100 s, the system achieved a MDL of 25.78 ppb. This study fully demonstrates the excellent spectroscopic sensing performance of the inverted-triangular LiNTF. In the future, the performance of LiNTF will be further enhanced by using gold electrodes and improved electrode adhesion processes to reduce signal loss.

References

1. Aliyu F, Sheltami T. Development of an energy-harvesting toxic and combustible gas sensor for oil and gas industries. *Sens Actuators B Chem* **231**, 265–275 (2016).
2. Zhang SY, Bi T, Del'Haye P. On-the-fly precision spectroscopy with a dual-modulated tunable diode laser and Hz-level referencing to a cavity. *Adv Photonics* **6**, 046003 (2024).
3. Li TG, Zhao PC, Wang P et al. Miniature optical fiber photoacoustic spectroscopy gas sensor based on a 3D micro-printed planar-spiral spring optomechanical resonator. *Photoacoustics* **40**, 100657 (2024).
4. Ma J, Fan EB, Liu HJ et al. Microscale fiber photoacoustic spectroscopy for in situ and real-time trace gas sensing. *Adv Photonics* **6**, 066008 (2024).
5. Wu GX, Zhu RZ, Lu YQ et al. Optical scanning endoscope via a single multimode optical fiber. *Opto-Electron Sci* **3**, 230041 (2024).
6. Shao MR, Ji C, Tan JB et al. Ferroelectrically modulate the Fermi level of graphene oxide to enhance SERS response. *Opto-Electron Adv* **6**, 230094 (2023).
7. Xu BX, Wan YY, Fan XY et al. Whispering-gallery-mode barcode-based broadband sub-femtometer-resolution spectroscopy with an electro-optic frequency comb. *Adv Photonics* **6**, 016006 (2024).
8. Kaloumenou M, Skotadis E, Lagopati N et al. Breath analysis: a promising tool for disease diagnosis—the role of sensors. *Sensors* **22**, 1238 (2022).
9. He Y, Qiao SD, Lang TE et al. Optical component-free dual-gas quartz-enhanced photoacoustic spectroscopy sensor based on highly integrated interband cascade lasers. *ACS Sens* **10**, 5238–5244 (2025).
10. Russo SD, Pelini J, Garcia IL et al. Dual-tube MEMS-based spectrophone for sub-ppb mid-IR photoacoustic gas detection. *Photoacoustics* **40**, 100644 (2024).
11. Nie QX, Peng YB, Chen QH et al. Agile cavity ringdown spectroscopy enabled by moderate optical feedback to a quantum cascade laser. *Opto-Electron Adv* **7**, 240077 (2024).
12. Li WH, Wang XY, Bayanheshig et al. Controlling the wavefront aberration of a large-aperture and high-precision holographic diffraction grating. *Light Sci Appl* **14**, 112 (2025).

13. Yin SY, Guo Q, Liu SR et al. Three-dimensional multichannel waveguide grating filters. *Opto-Electron Sci* **3**, 240003 (2024).
14. Sun XR, Sun HY, He Y et al. An ultrahighly sensitive CH_4-TDLAS sensor based on an 80-m optical path length multipass cell with a dense circular spot pattern. *Anal Chem* **97**, 10886–10892 (2025).
15. Liu C, Wang G, Zhang C et al. End-to-end methane gas detection algorithm based on transformer and multi-layer perceptron. *Opt Express* **32**, 987–1002 (2024).
16. Wang YZ, He Y, Qiao SD et al. Fast step heterodyne light-induced thermoelastic spectroscopy gas sensing based on a quartz tuning fork with high-frequency of 100 kHz. *Opto-Electron Adv* **9**, 250150 (2026).
17. Qiu XB, Xiong XH, Li L et al. Development of an FDM-TDLAS sensor for long-term online monitoring of H_2S and CO to predict water wall corrosion trends. *Anal Chem* **97**, 14058–14066 (2025).
18. Wijesinghe DR, Zobair MA, Esmaeelpour M. A review on photoacoustic spectroscopy techniques for gas sensing. *Sensors* **24**, 6577 (2024).
19. Li TL, Sima CT, Ai Y et al. Photoacoustic spectroscopy-based ppb-level multi-gas sensor using symmetric multi-resonant cavity photoacoustic cell. *Photoacoustics* **32**, 100526 (2023).
20. Gong ZF, Fan YM, Guan YC et al. Empirical modal decomposition combined with deep learning for photoacoustic spectroscopy detection of mixture gas concentrations. *Anal Chem* **96**, 18528–18536 (2024).
21. Kosterev AA, Bakhirkin YA, Curl RF et al. Quartz-enhanced photoacoustic spectroscopy. *Opt Lett* **27**, 1902–1904 (2002).
22. Ma YF, Qiao SD, Wang RQ et al. A novel tapered quartz tuning fork-based laser spectroscopy sensing. *Appl Phys Rev* **11**, 041412 (2024).
23. Zifarelli A, Negro G, Mongelli LA et al. Effect of gas turbulence in quartz-enhanced photoacoustic spectroscopy: a comprehensive flow field analysis. *Photoacoustics* **38**, 100625 (2024).
24. Li CN, He Y, Qiao SD et al. A low-cost full-range hydrogen sensor based on quartz tuning fork. *IEEE Sens J* **25**, 16943–16949 (2025).
25. Li JS, Liu NW, Ding JY et al. Piezoelectric effect-based detector for spectroscopic application. *Opt Lasers Eng* **115**, 141–148 (2019).
26. Sang CZ, Zhang C, Wang RQ et al. Tapered acoustic resonator-based quartz-enhanced photoacoustic spectroscopy. *Opt Lett* **50**, 4646–4649 (2025).
27. Chen YJ, Ma HX, Qiao SD et al. Rapid ppb-Level methane detection based on quartz-enhanced photoacoustic spectroscopy. *Anal Chem* **97**, 6780–6787 (2025).
28. Qiao SD, He Y, Sun HY et al. Ultra-highly sensitive dual gases detection based on photoacoustic spectroscopy by exploiting a long-wave, high-power, wide-tunable, single-longitudinal-mode solid-state laser. *Light Sci Appl* **13**, 100 (2024).
29. Zhang C, Qiao SD, He Y et al. Double resonant quartz-enhanced photoacoustic spectroscopy with a spherical resonator. *Opt Lett* **50**, 3776–3779 (2025).
30. Kinjalk K, Paciolla F, Sun B et al. Highly selective and sensitive detection of volatile organic compounds using long wavelength InAs-based quantum cascade lasers through quartz-enhanced photoacoustic spectroscopy. *Appl Phys Rev* **11**, 021427 (2024).
31. Sun J, He Y, Qiao SD et al. Acetylene-enhanced methane-QEPAS sensing. *Opt Lett* **50**, 3760–3763 (2025).
32. Yang X, Zhang C, Qiao SD et al. Non-resonant quartz-enhanced photoacoustic spectroscopy. *Chin Opt Lett* **23**, 093002 (2025).
33. Zhang L, Zhen YQ, Tong LM. Optical micro/nanofiber enabled tactile sensors and soft actuators: a review. *Opto-Electron Sci* **3**, 240005 (2024).
34. Qiao SD, Liu XN, Lang ZT et al. Quartz-enhanced laser spectroscopy sensing. *Light Sci Appl* (2026). doi: 10.1038/s41377-025-02075-7.
35. Sampaolo A, Yu CR, Wei TT et al. H_2S quartz-enhanced photoacoustic spectroscopy sensor employing a liquid-nitrogen-cooled THz quantum cascade laser operating in pulsed mode. *Photoacoustics* **21**, 100219 (2021).
36. Sun HY, Qiao SD, He Y et al. Parts-per-quadrillion level gas molecule detection: CO-LITES sensing. *Light Sci Appl* **14**, 180 (2025).
37. Zifarelli A, Sampaolo A, Patimisco P et al. Methane and ethane detection from natural gas level down to trace concentrations using a compact mid-IR LITES sensor based on univariate calibration. *Photoacoustics* **29**, 100448 (2023).
38. Lang ZT, Qiao SD, Ma YF. Fabry–Perot-based phase demodulation of heterodyne light-induced thermoelastic spectroscopy. *Light Adv Manuf* **4**, 23(2023).
39. He Y, Wang YZ, Qiao SD et al. Hydrogen-enhanced light-induced thermoelastic spectroscopy sensing. *Photonics Res* **13**, 194–200 (2025).
40. Russo SD, Zifarelli A, Patimisco P et al. Light-induced thermoelastic effect in quartz tuning forks exploited as a photodetector in gas absorption spectroscopy. *Opt Express* **28**, 19074–19084 (2020).
41. Wang RQ, Guan XY, Qiao SD et al. Ultrahigh sensitive LITES sensor based on a trilayer ultrathin perfect absorber coated T-head quartz tuning fork. *Laser Photonics Rev* **19**, 2402107 (2025).
42. Liu YH, Qiao SD, Fang C et al. A highly sensitive LITES sensor based on a multi-pass cell with dense spot pattern and a novel quartz tuning fork with low frequency. *Opto-Electron Adv* **7**, 230230 (2024).
43. Hu LE, Zheng CT, Zhang MH et al. Long-distance in-situ methane detection using near-infrared light-induced thermo-elastic spectroscopy. *Photoacoustics* **21**, 100230 (2021).
44. Sun HY, Liu YH, He Y et al. Highly sensitive CH_4/C_2H_2 dual-gas light-induced thermoelastic spectroscopy sensor based on a dual-path multiring multipass cell and a circle-head quartz tuning fork. *ACS Sens* **10**, 4717–4724 (2025).
45. Qiao SD, Lang ZT, He Y et al. Calibration-free measurement of absolute gas concentration and temperature via light-induced thermoelastic spectroscopy. *Adv Photonics* **7**, 066007 (2025).
46. Sun B, Patimisco P, Sampaolo A et al. Light-induced thermoelastic sensor for ppb-level H_2S detection in a SF_6 gas matrices exploiting a mini-multi-pass cell and quartz tuning fork photodetector. *Photoacoustics* **33**, 100553 (2023).
47. Ma HX, Sun XR, Qiao SD et al. A high-performance light-induced thermoelastic spectroscopy sensor based on a high-Q value quartz tuning fork load. *Sens Actuators B Chem* **436**, 137713 (2025).
48. Sun HY, He Y, Qiao SD et al. Highly sensitive and real-simultaneous CH_4/C_2H_2 dual-gas LITES sensor based on Lissajous pattern multi-pass cell. *Opto-Electron Sci* **3**, 240013 (2024).
49. Ma YM, Sui X, Song F et al. Optical-domain modulation cancel-

lation method for background-suppression and dual-gas detection in light-induced thermo-elastic spectroscopy. *Sens Actuators B Chem* **404**, 135168 (2024).

50. Wang RQ, Qiao SD, He Y et al. Highly sensitive laser spectroscopy sensing based on a novel four-prong quartz tuning fork. *Opto-Electron Adv* **8**, 240275 (2025).
51. Patimisco P, Sampaolo A, Dong L et al. Analysis of the electro-elastic properties of custom quartz tuning forks for optoacoustic gas sensing. *Sens Actuators B Chem* **227**, 539–546 (2016).
52. Ma YF, Liu YH, He Y et al. Design of multipass cell with dense spot patterns and its performance in a light-induced thermoelastic spectroscopy-based methane sensor. *Light Adv Manuf* **6**, 1(2025).
53. Shang ZJ, Wu HP, Wang G et al. Robust and compact light-induced thermoelastic sensor for atmospheric methane detection based on a vacuum-sealed subminiature tuning fork. *Photoacoustics* **42**, 100691 (2025).
54. Ma YF, Sun XR, Sun HY et al. An ultra-highly sensitive LITES sensor based on multi-pass cell with ultra-dense spot pattern designed by multi-objective algorithm. *PhotoniX* **6**, 26 (2025).
55. Dai JL, Wang CY, Liu PH et al. Sensitive light-induced thermoelastic spectroscopy-based oxygen sensor with a Perovskite-modified quartz tuning fork. *IEEE Sens J* **23**, 22380–22388 (2023).
56. Lou CG, Wang Y, Zhang Y et al. Reduced graphene oxide/polydimethylsiloxane as an over-coating layer on quartz tuning fork for sensitive light-induced thermoelastic spectroscopy. *IEEE Sens J* **22**, 10459–10464 (2022).
57. Zhou S, Xu LG, Chen K et al. Absorption spectroscopy gas sensor using a low-cost quartz crystal tuning fork with an ultrathin iron doped cobaltous oxide coating. *Sens Actuators B Chem* **326**, 128951 (2021).
58. Zou YT, Zhou SL, Li JX et al. A mid-infrared perfect metasurface absorber with tri-band broadband scalability. *Nanomaterials* **14**, 1316 (2024).
59. Weis RS, Gaylord TK. Lithium niobate: summary of physical properties and crystal structure. *Appl Phys A* **37**, 191–203 (1985).
60. Weng WS. Electromechanical coupling coefficients for some modes of vibration of lithium niobate single crystal. *Acta Acust* **10**, 180–189 (1985).
61. Wang Y, Jiang YJ. Crystal orientation dependence of piezoelectric properties in $LiNbO_3$ and $LiTaO_3$. *Opt Mater* **23**, 403–408 (2003).
62. Tang M, Chen DH, Zhang M et al. Optimized design of lithium niobate tuning forks for the measurement of fluid characteristic parameters. *Micromachines* **14**, 2138 (2023).
63. Ono K, Yachi M, Wakatsuki N. H-type single crystal piezoelectric gyroscope of an oppositely polarized $LiNbO_3$ plate. *Jpn J Appl Phys* **40**, 3699–3703 (2001).
64. Turutin AV, Vidal JV, Kubasov IV et al. Highly sensitive magnetic field sensor based on a metglas/bidomain lithium niobate composite shaped in form of a tuning fork. *J Magn Magn Mater* **486**, 165209 (2019).
65. Chen KF, Zhu Y, Liu Z et al. State of the art in crystallization of $LiNbO_3$ and their applications. *Molecules* **26**, 7044(2021).
66. Cantatore AFP, Menduni G, Zifarelli A et al. Lithium niobate-enhanced photoacoustic spectroscopy. *Photoacoustics* **35**, 100577 (2024).

Acknowledgements

This work was supported by the National Natural Science Foundation of China (Grant Nos. 62335006, 62275065, 62022032, 62405078, and 62505066), Open Subject of Hebei Key Laboratory of Advanced Laser Technology and Equipment (Grant No. HBKL-ALTE2025001), Heilongjiang Postdoctoral Fund (Grant No. LBH-Z23144 and LBH-Z24155), Natural Science Foundation of Heilongjiang Province (Grant No. LH2024F031), China Postdoctoral Science Foundation (Grant No. 2024M764172).

Author contributions

Yufei Ma supervised the whole project and revised the manuscript. Junjie Mu performed the measurements and wrote the original manuscript. Junjie Mu, Guowei Han, Runqiu Wang, Shunda Qiao and Ying He involved in the investigations.

Competing interests

The authors declare no competing financial interests.

Scan for Article PDF